Fuel 425 (2026) 139516

Contents lists available at ScienceDirect

Fuel

journal homepage: www.elsevier.com/locate/jfue

Full length article

Characterisation of multi-stage self-ignition of iron particle clouds in sheared turbulence

Tien Duc Luu*, Marlon Göhringer, David Märker, Oliver T. Stein

Engler-Bunte-Institut (EBI), Simulation of Reacting Thermo-Fluid Systems (TFS), Karlsruhe Institute of Technology (KIT), Engler-Bunte-Ring 7, 76131 Karlsruhe, Germany

HIGHLIGHTS

- Fundamental carrier-phase DNS to analyse and quantify iron particle self-ignition stages under various ambient conditions.
- Characterising particle ignition-stages in shear-driven turbulence.
- Identifying key parameters to control the iron self-ignition behaviour.
- Fundamental trends found here can help to indicate optimised self-ignition conditions in future iron particle combustors.

ARTICLE INFO

Keywords:
Iron particle combustion
Solid fuel combustion
Metal fuel
CP-DNS
Self-ignition
Turbulence
Mixing layer

ABSTRACT

In this paper, a three-dimensional carrier-phase direct numerical simulation (CP-DNS) approach is employed to analyse the self-ignition conditions of reacting iron particle clouds in sheared turbulence, i.e., a reacting mixing layer. The gas phase is described by the Eulerian transport equations for mass, momentum, sensible enthalpy and chemical species, while the solid phase follows the Lagrangian equations for particle mass, momentum and temperature. The interaction between the two phases is realised through interphase coupling terms. Various operating conditions are tested by adapting the key parameters for the ignition and combustion process, namely gas temperature, oxygen mass fraction, equivalence ratio and particle diameter. Moreover, the effect of radiation is explored, as well as the impact of initialising the lower stream of the mixing layer with fully-oxidised particles. The particle self-ignition behaviour is characterised in terms of the spatially-averaged gas temperature, the total heat released by the particles and the gradient of the latter. Starting from a reference case, one key parameter is changed at a time to isolate its individual effects. The results reveal that two distinct ignition stages with different times occur under most conditions. Under specific conditions, the first and second stages merge, resulting in a single global cloud ignition time. Significant impacts on the self-ignition behaviour are observed for the initial gas phase temperature and particle diameter, while the effects of the oxygen concentration, particle equivalence ratio and the inclusion of radiation are smaller. The addition of fully-oxidised particles to the lower stream does not show any substantial effect on the global ignition behaviour of the iron particle combustion system. Despite being derived for well-controlled, synthetic conditions and using simplified sub-models, the trends identified in this study may serve as a first indicator for controlling iron particle cloud combustion and determining optimised operating conditions for stable self-ignition in future iron particle combustors.

1. Introduction

As the global population and industrial development increase, the world's energy supply is also expected to rise. While fossil fuels remain the primary energy source, their environmental impact raises the need for alternatives. Renewable and carbon-free energy sources are wind and solar. However, their uneven geographical distribution and high fluctuations make it challenging to provide a consistent energy supply to regions with high demand. A potential solution is adopting carbon-free energy storage systems. A promising technology is the oxidation of iron, combined with the reverse iron oxide reduction process based on renewable energy [1,2]. Iron has a high energy density, is globally abundant, and provides good transport and storage properties. Iron oxidation

* Corresponding author.
Email address: tien.luu@kit.edu (T.D. Luu).

https://doi.org/10.1016/j.fuel.2026.139516
Received 8 February 2026; Received in revised form 2 April 2026; Accepted 14 April 2026
Available online 17 April 2026

differs from conventional solid fuel conversion processes (e.g., coal or biomass) as it typically oxidises fully heterogeneously. The physical processes differ in such a way that existing models for volatile-containing solid fuels require modification or need to be newly developed to become applicable to iron.

A first simplified analytical model to predict the heating, ignition and diffusive burnout of metal particles has been proposed by Goroshin et al. [3]. Recently, Soo et al. [4] suggested a model considering the kinetic and diffusion regimes during iron combustion. Hazenberg and van Oijen [5], Thijs et al. [6] and Mich et al. [7] further developed the model by Soo et al. [4] by improving the heat and mass transfer [6] and investigating polydispersity effects [7]. Further numerical studies have been conducted to study the discreteness [8–10], flame structure and laminar burning velocities [5,11,12], clustering effects [13–15] and nanoparticle formation [16]. Several experimental studies under laminar conditions have been conducted for single iron particles [17,18] and iron particle clouds [19–21] in the past few years.

The development of iron combustion technologies for industrial systems is still in its early stages, leading to extensive numerical as well as experimental research efforts to explore the underlying chemical and physical processes. Developing industrial iron oxidation systems is associated with several challenges, e.g., combustor design, degree of turbulence and operating conditions, which affect the ignition and stabilisation of heterogeneous iron flames in air. Experimental studies have shown that for specific process parameters, stable ignition and combustion of iron particles can only be obtained by gas-assisted ignition using e.g., methane [20]. However, stable self-ignition of iron particles in air can also be achieved [19,21] and is preferred. Moreover, the characterisation of heterogeneous ignition in iron-air systems is not trivial since it differs significantly from the ignition of typical solid hydrocarbon fuels with volatiles as no radicals are involved in these processes. To investigate these phenomena in detail, the carrier-phase direct numerical simulation (CP-DNS) approach provides a good trade-off between accuracy and efficiency for iron particle cloud combustion [13–15,22]. A suitable canonical configuration for studying the non-premixed ignition and combustion process is the mixing layer setup [15,22]. Mixing layer configurations attempt to capture the essential physics that occur near industrial burner inlets. These conditions cannot be reproduced using simplified single particle configurations. The important processes controlling ignition include particle heating, oxygen diffusion towards the particle surface, particle kinetics as well as turbulent mixing and clustering effects. These interacting processes can only be described accurately by CP-DNS of turbulent, reacting two-phase mixing layers. Here, we extend our previous work on iron particle clouds in turbulent mixing layers [13,22] to analyse self-ignition conditions in turbulent environments by varying the gas temperature, oxygen concentration and radiation characteristics, as well as the particle diameter and particle loading. Moreover, we characterise the various ignition stages which occur in sheared turbulence. The objectives of the present study are to

- analyse and quantify the self-ignition of iron particles under various ambient conditions,
- identify the key parameters of self-ignition,
- characterise particle ignition stages in shear-driven turbulence.

2. Modelling

2.1. Gas phase

The governing equations of gas mass, momentum, enthalpy and species read

$$\frac{\partial \rho}{\partial t} + \frac{\partial (\rho u_i)}{\partial x_i} = \dot{S}_{\rho,p} \tag{1}$$

$$\frac{\partial (\rho u_i)}{\partial t} + \frac{\partial (\rho u_i u_j)}{\partial x_j} = -\frac{\partial p}{\partial x_i} + \frac{\partial}{\partial x_j}\left[\mu\left(\frac{\partial u_j}{\partial x_i} + \frac{\partial u_i}{\partial x_j}\right) - \frac{2}{3}\mu\frac{\partial u_m}{\partial x_m}\delta_{ij}\right] + \dot{S}_{u,p} \tag{2}$$

$$\frac{\partial (\rho h_s)}{\partial t} + \frac{\partial (\rho h_s u_j)}{\partial x_j} = \frac{\partial}{\partial x_j}\left(\frac{\mu}{\mathrm{Pr}}\frac{\partial h_s}{\partial x_j}\right) + \dot{S}_{\mathrm{rad}} + \dot{S}_{h_s,p} \tag{3}$$

$$\frac{\partial (\rho Y_k)}{\partial t} + \frac{\partial (\rho Y_k u_j)}{\partial x_j} = \frac{\partial}{\partial x_j}\left(\frac{\mu}{\mathrm{Sc}}\frac{\partial Y_k}{\partial x_j}\right) + \dot{\omega}_k + \dot{S}_{Y_k,p} \tag{4}$$

Here, subscripts $< i, j, m >$ indicate the coordinate directions, ρ the density, t the time, x the spatial coordinate, u the velocity, h_s the sensible enthalpy and Y_k the mass fraction of species k. p represents the pressure, δ_{ij} the Kronecker delta and μ the dynamic viscosity. Le = 1 is assumed with the Schmidt and Prandtl numbers for mass and heat diffusivities Sc = Pr = 0.7. $\dot{S}_{\mathrm{rad}}$ denotes the radiative source term retrieved from the discrete ordinate method (DOM) considering 80 rays. Pure air is assumed to be transparent and does not absorb or emit radiation ($\varepsilon_{\mathrm{gas}} \approx 0.001$), while isotropic particle scattering is considered. Since no nanoparticle formation occurs, homogeneous gas phase chemistry is omitted ($\dot{\omega}_k = 0$). The gas-solid interphase source terms in Eqs. (1)–(4) are closed as

$$\dot{S}_{\rho,p} = -\frac{1}{\Delta^3}\sum_{p=1}^{N_p}\frac{dm_p}{dt}, \tag{5}$$

$$\dot{S}_{u,p} = -\frac{1}{\Delta^3}\sum_{p=1}^{N_p}\frac{d(m_p \mathbf{u}_p)}{dt}, \tag{6}$$

$$\dot{S}_{h_s,p} = -\frac{1}{\Delta^3}\sum_{p=1}^{N_p}\left(\frac{m_p c_{\mathrm{p},p}}{\tau_{\mathrm{con}}}(T_g - T_p) + \frac{dm_p}{dt}h_{s,\mathrm{O_2}}|_{T_p}\right) \tag{7}$$

$$\dot{S}_{Y_k,p} = \dot{S}_{\mathrm{O_2},p} = \dot{S}_{\rho,p} \tag{8}$$

with subscripts $\langle p \rangle$ and $\langle g \rangle$ indicating particle and gas properties, respectively. m is the mass, T the temperature, $\mathbf{u}$ the velocity vector, c_{p} the specific heat capacity, τ_{con} the convective heat transfer time scale, $h_{s,\mathrm{O_2}}|_{T_p}$ the sensible enthalpy of consumed oxygen during oxidation at T_p and N_p the number of particles in the local cell with cell size Δ.

2.2. Solid phase

The iron particles are initialised as Lagrangian point-particles and the solid phase governing equations are given as

$$\frac{dm_p}{dt} = \frac{dm_{p,\mathrm{Fe}}}{dt} + \frac{dm_{p,\mathrm{FeO}}}{dt}, \tag{9}$$

$$\frac{d\mathbf{u}_p}{dt} = \frac{\mathbf{u}_g - \mathbf{u}_p}{\tau_p}, \tag{10}$$

$$\frac{dT_p}{dt} = \frac{1}{\tau_{\mathrm{con}}}(T_g - T_p) + \frac{\varepsilon_p A_p \sigma}{m_p c_{\mathrm{p},p}}(\Theta_r^4 - T_p^4) + \frac{\dot{Q}_{\mathrm{FeO}}}{m_p c_{\mathrm{p},p}} + \frac{\dot{Q}_{\mathrm{O_2}}}{m_p c_{\mathrm{p},p}} \tag{11}$$

with $\tau_p = \frac{\rho_p d_p^2}{18\mu_f}(1 + 0.15\mathrm{Re}_p^{2/3})^{-1}$ the particle relaxation time with subscript $\langle f \rangle$ denoting film properties. $A_p = \frac{1}{4}\pi d_p^2$ is the projected area of the particle, $\varepsilon_p = 0.9$ the particle emissivity, σ the Stefan-Boltzmann constant, Θ_r the gas radiation temperature retrieved from DOM, $\dot{Q}_{\mathrm{FeO}} = \frac{dm_{p,\mathrm{FeO}}}{dt}\Delta h_{c,\mathrm{FeO}}$ the heat released by Fe oxidation, $\Delta h_{c,\mathrm{FeO}}$ the formation enthalpy of FeO, and $\dot{Q}_{\mathrm{O_2}}$ the energy transfer due to oxygen consumption at T_p. The convective heat transfer time scale is calculated according to

$$\tau_{\mathrm{con}} = \frac{1}{6}\frac{\mathrm{Pr}}{\mathrm{Nu}^*}\frac{c_{\mathrm{p},p}}{c_{\mathrm{p},f}}\frac{\rho_p d_p^2}{\mu_f} \tag{12}$$

with the Nusselt number Nu* corrected for Stefan flow [22]. The oxidation of iron follows

$$\mathrm{Fe} + 0.5\mathrm{O_2} \rightarrow \mathrm{FeO}. \tag{13}$$

The densities of Fe (solid or liquid) and FeO (solid or liquid) are calculated similarly to [7] and the remaining thermophysical properties are

retrieved from [23] by using the Shomate equations. Melting and solidification of Fe and FeO is considered with the heat capacity method [24]. The total particle specific heat capacity is obtained from the individual heat capacities of Fe and FeO as $c_{p,p} = Y_{Fe}c_{p,Fe} + Y_{FeO}c_{p,FeO}$. The iron conversion sub-model reads [7]

$$\frac{dm_{p,Fe}}{dt} = -\frac{1}{s}\rho_f Y_{O_2} A_d k_d \mathrm{Da}^*, \tag{14}$$

$$\frac{dm_{p,FeO}}{dt} = \frac{1+s}{s}\rho_f Y_{O_2} A_d k_d \mathrm{Da}^*, \tag{15}$$

where,

$$\mathrm{Da}^* = \frac{A_r k_r}{A_r k_r + A_d k_d} \tag{16}$$

represents the normalised Damköhler number. $A_r = A_d = \pi d_p^2$ denote the reactive and diffusive areas of the particle, $k_r = k_\infty e^{-E_a/R_u T_p}$ the rate of kinetic surface reactions and $k_d = \mathrm{Sh}^* \frac{D_{O_2,f}}{d_p}$ the diffusive oxygen transfer rate. Sh^* is the corrected Sherwood number due to Stefan flow [22], $\mathrm{Re}_p = \rho_f |\mathbf{u}_g - \mathbf{u}_p| \frac{d_p}{\mu_f}$ the particle Reynolds number and s the mass stoichiometric ratio of the oxidation to FeO. The corrected Nu^* and Sh^* are based on the Ranz-Marshall correlations that are functions of Re_p. The range of the latter has been identified for the present setup in our previous work [22] and lies within the validity range of the applied corrections [25,26]. Similar correlations and corrections have been previously applied under comparable turbulence intensities ($\Delta u_x = 20 \dots 30$ m/s and $\frac{T_{US}+T_{LS}}{2} = 1100 \dots 1400$ K) for reacting mixing layers with droplet evaporation/combustion [27] and solid fuel combustion [15,28–30]. Remaining model coefficients are based on [7]. The present implementation of the sub-models for iron particle oxidation has been validated against laser-ignited single particle combustion experiments [17,24], reproducing the temporal evolution of particle temperature throughout the oxidation process. In addition, the predicted time to peak particle temperature agrees well with the experimental data of [17] and with numerical solutions from [7] over a wide range of oxygen concentrations and particle diameters, as demonstrated in our previous work [13,22]. Overall, the present sub-models accurately reproduce both the particle temperature evolution and the time to peak temperature and are therefore suited for analysing the particle self-ignition process. Mi et al. [31] and others have proposed alternative iron conversion sub-models that also describe the higher oxidation states of iron and further physical effects. Van Gool et al. [32] extended the iron conversion sub-model [5,7] to include higher oxidation states (Fe_2O_3 and Fe_3O_4). Their results indicate that the oxidation to FeO accounts for most of the heat release and remains the dominant reaction up to the point where the particle reaches its peak temperature. Beyond this point, reactions involving higher oxides become more prominent and release the remaining heat during the reactive cooling phase [32,33]. Nevertheless, the particle temperature continues to decrease as heat losses to the surroundings exceed the heat generated by the formation of higher oxidation states. Neglecting the formation of higher oxides results in slightly reduced heat release, faster particle cooling and a delay of the subsequent processes (e.g., the second ignition stage, see Section 4.1). However, in the present work, since we solely focus on the initial heat-up, mixing and ignition stages of the particles -during which the conversion of Fe to FeO is most prominent- we limit ourselves to the simplified iron conversion sub-model of Mich et al. [7]. This choice covers the most relevant oxidation physics here and ensures consistency with our previous research and offers a high computational efficiency within our CP-DNS framework.

3. Computational setup

The present mixing layer setup is similar to our previous work [13,22] and is based on the momentum thickness δ_θ. The upper stream (US) of the mixing layer consists of 'cold' air ($Y_{O_2} = 0.233$, $Y_{N_2} = 0.767$). The 'hot' lower stream (LS) is composed of a variation of Y_{O_2}/Y_{N_2} at various T_{LS}. The velocity of both streams is equal but points in the opposite x-direction with a difference $\Delta u_x = 30$ m/s, as shown in Fig. 1. Following [34], a hyperbolic tangent profile is used to initialise velocity u_x as

$$u_x = \frac{\Delta u_x}{2} \tanh\left(\frac{y - L_y/2}{2\delta_{\theta,0}}\right). \tag{17}$$

The initial momentum thickness $\delta_{\theta,0}$ results from the Reynolds number

$$\mathrm{Re}_{\theta,0} = \frac{\Delta u_x \delta_{\theta,0}}{(\nu_{US} + \nu_{LS})/2} = 44.018 \tag{18}$$

with ν_{US} and ν_{LS} being the initial viscosities of the upper and lower stream, respectively. Based on the momentum thickness, the computational domain spans over $L_x = 320 \times \delta_{\theta,0}$, $L_y = 240 \times \delta_{\theta,0}$ and $L_z = 80 \times \delta_{\theta,0}$. The domain is divided into ≈ 85 M cubic cells, resulting in a cell size of $\Delta = 100\,\mu$m. Monodisperse spherical iron particles with $T_p = T_{US}$ and $\mathbf{u}_p = \mathbf{u}_{US}$ are initialised in the US. For most conditions the lower stream does initially not have any particles, while for one of our studies we explore the impact of recirculating fully-oxidised iron particles (FeO) in the lower stream. To speed up the mixing of both streams, isotropic velocity perturbations $u'u' = v'v' = w'w' = 0.01(\Delta u_x)^2$ with a size of $0.01 \cdot L_x$ are initially superimposed at $y/L_y = 0.5$ with a height of $4 \cdot \delta_{\theta_0}$ and exponentially decrease to zero for large $|\ y\ |$. Periodic boundary conditions are applied in x- and z-direction, while zero-gradient (ambient pressure) boundary conditions are assumed in y-direction for momentum and energy (pressure).

To characterise the multi-stage self-ignition of iron particle clouds, a variation of the key quantities that govern the ignition process is explored. The related cases are summarised in Table 1. Starting from the reference case [22], only one parameter is changed at a time, to isolate its individual effect.

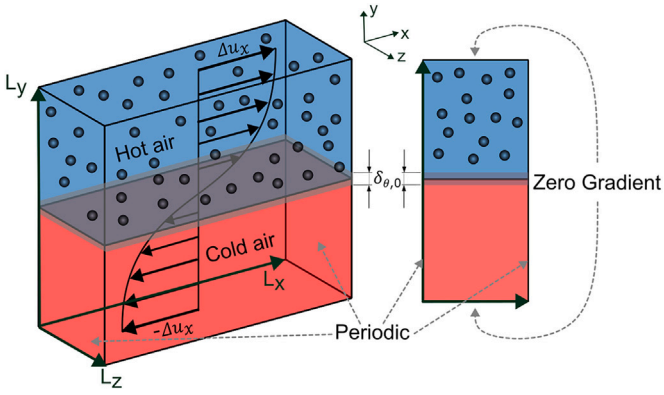

Fig. 1. Initial and boundary conditions of the mixing layer.

Table 1
Key parameters for iron particle cloud self-ignition, with T_{LS} and Y_{LS,O_2} the gas temperature and O_2 mass fraction of the lower stream, d_p the particle diameter, ϕ_{US} the upper stream equivalence ratio, $n_{p,FeO}$ the fraction of fully-oxidised particles in the lower stream, and the inclusion of radiation (Rad.).

			Ref. case	
T_{LS} in K	900	1200	1650	2000
Y_{LS,O_2}	0.0	0.1	0.233	–
d_p in µm	–	7.5	10	15
ϕ_{US}	–	0.5	1.0	1.5
$n_{p,FeO}$ in %	25	50	0.0	–
Rad.	–	off	on	–

We further identified the key non-dimensional parameters controlling particle ignition as the particle Nusselt number Nu_p (particle heating), particle Sherwood number Sh_p (oxygen availability and diffusion), equivalence ratio ϕ (fuel loading) and the normalised Voronoi volume v/v_{mean} (particle spacing/clustering). However, due to the strong coupling between the physical processes governed by these parameters, a truly systematic and independent non-dimensional variation seems unfeasible.

The CP-DNS approach is valid if the grid size follows

$$d_p \ll \Delta < \eta, \tag{19}$$

such that all relevant turbulent scales are resolved (η: Kolmogorov length scale), while the Lagrangian point-particle assumption remains valid and we keep the same ranges as in our previous work [22]. It should also be noted that classical grid independence cannot be fully achieved in Euler-Lagrange approaches, since Eq. (19) must remain satisfied throughout the simulation for particle diameters of $d_p = [7.5, 10, 15]$ µm. The simulations are conducted with an in-house low-Mach multiphase finite volume solver based on OpenFOAM-v2012. To reduce numerical errors associated with the Lagrangian point-particle formulation, see Eqs. (9)–(11), a sub-time-stepping scheme is employed, in which the particle mass is updated after each sub-step. A typical CP-DNS run costs ≈ 165,225 CPUh on 1024 × Intel Xeon Platinum 8358 cores.

4. Results and discussion

4.1. Reference case

A visual representation of the reference case defined in Table 1 is shown in Fig. 2 at $t = 1.75$ and $t = 3$ ms. The top row illustrates the gas temperature with iso-surfaces at $T = 1000$ K and $T = 1700$ K, while the bottom row shows the particles, coloured by their extent of iron oxidation, represented by $C_{ox} = \frac{m_{Fe,0} - m_{Fe}}{m_{Fe,0}}$, with $m_{Fe,0}$ and $m_{Fe,t}$ denoting the initial and instantaneous iron mass in the particle. Initially the two streams are separated, with particles present in the US. As time progresses, a mixing region develops at $L_y/2$, with particles that are entrained by the flow field. At $t = 1.75$ ms, particles are entrained from the US to LS, leading to an increase in particle temperature and initiating the oxidation of individual particles ($C_{ox} > 0.0$ - grey/white) which in turn releases heat due to the exothermic reaction. However, the gas temperature plot at $t = 1.75$ ms (top row) shows no noticeable impact of the particle heat release, indicating that this heat is insufficient to affect the gas temperature significantly, but may primarily serve to heat up the surrounding particles. At $t = 3$ ms, regions of the gas phase with temperatures exceeding the initialisation temperature (> 1650 K) can be identified by the red colour. The particle plot reveals that a high number of particles are now coloured grey… white, indicating that a significant heat release from a large number of particles is needed to substantially influence the gas phase. Such particle clustering effects have already been observed in [13–15]. Particles with Stokes number St → 1 have a stronger tendency to cluster [13,15] and such turbulent clustering has been associated with faster ignition [14]. Fig. 3 illustrates this effect, where clustered particles ($v/v_{mean} < 1$, based on the Voronoi volume v and its mean inside the domain v_{mean} [13,14]) oxidise collectively ($C_{ox} > 0$) and lead to higher local gas temperatures. At $t = 1$ ms, particles are clustered but not yet ignited, whereas at $t = 3$ ms, ignition within these clusters (mostly for $v/v_{mean} < 1$) leads to an increase in gas temperature. This observation is supported by Fig. 4, where the top row shows the oxidation state of particles along the normalised y-axis at $t = 1.75$ and 3 ms. The bottom row considers only reactive particles with $0.05 < C_{ox} < 0.95$, confirming that many more particles are involved in the oxidation process at $t = 3$ ms compared to $t = 1.75$ ms, as a result of the growing turbulent eddy structures indicated by the wider spread at $t = 3$ ms.

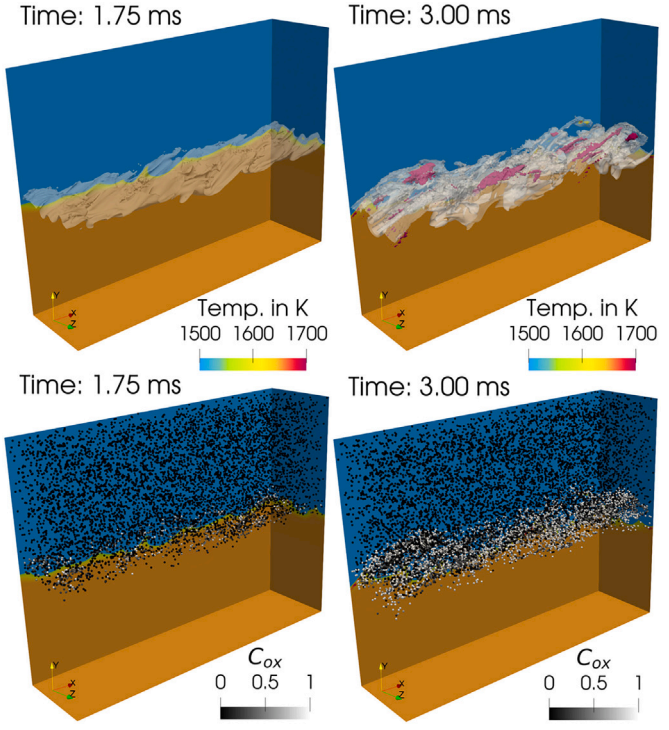

Fig. 2. Time evolution of the reference case until $t = 3$ ms. Top: Gas temperature with iso-surfaces at $T = 1000$ K and $T = 1700$ K. Bottom: Particle cloud coloured by its oxidation progress C_{ox} (scaled in size for visualisation purposes). (For interpretation of the references to colour in this figure legend, the reader is referred to the web version of this article.)

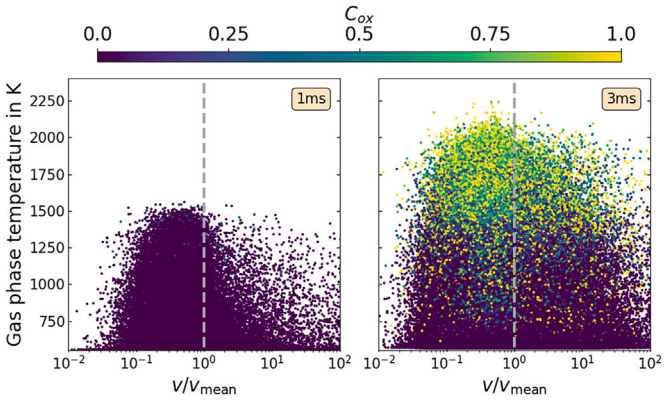

Fig. 3. Ref. case - Scatterplot of gas temperature T vs. normalised Voronoi volume v/v_{mean} coloured by C_{ox} at different times. (For interpretation of the references to colour in this figure legend, the reader is referred to the web version of this article.)

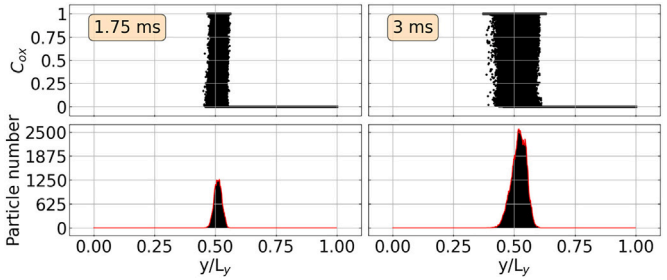

Fig. 4. Ref. case - Top: Scatterplot of C_{ox} vs. normalised cross-stream coordinate y. Bottom: Number of reactive particles with $0.05 < C_{ox} < 0.95$.

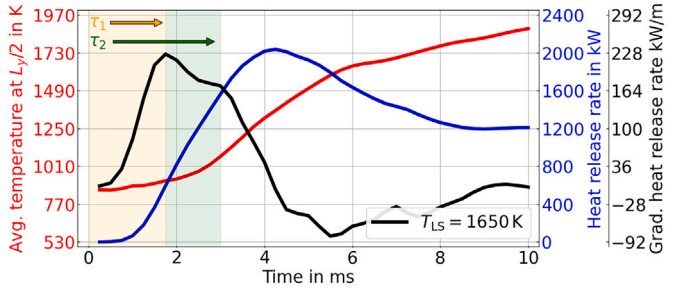

Fig. 5. Ref. case - spatially-averaged gas temperature T_{avg} at $L_y/2$ (red), particle heat release rate $\dot{Q}_t$ (blue) and gradient of particle heat release rate $d\dot{Q}_t$ (black) vs. time t. τ_1 and τ_2 indicate the ignition times. (For interpretation of the references to colour in this figure legend, the reader is referred to the web version of this article.)

Fig. 5 assesses the observed behaviour more quantitatively by plotting the spatially-averaged gas temperature T_{avg} (red), total particle heat release rate at the given time step $\dot{Q}_t$ (blue) and the corresponding gradient $d\dot{Q}_t$ (black). The gas temperature averaging procedure follows the method outlined in [22], where only the gas temperature at $L_y/2$ is considered and shown in Fig. 5, as the major events occur at this position. The total heat release rate plotted in blue is derived from $\dot{Q}_{FeO}$ in the third term on the right-hand side of Eq. (11), summed over all particles. Between $0 < t < 1$ ms no oxidation of the iron particles occurs. Starting at $t > 1$ ms, the particles begin their oxidation process, releasing heat until reaching the peak at $t = 4$ ms and equilibrating at ≈ 1200 kW at late times. The increase in the heat release between $1 < t < 4$ ms is not a steady rise but instead involves dynamic changes in the slopes due to the discrete and heterogeneous nature of metal fuels. To better visualise these changes in slope, the gradient of the heat release is plotted in black. This indicates two distinct particle ignition times at $\tau_1 = 1.75$ ms and $\tau_2 = 3$ ms, based on a similar ignition definition $\partial^2 \sum_p^{N_p} \dot{Q}_{pFeO}/\partial t^2 \approx 0$ in [35]. In the absence of nanoparticle formation, it is reasonable to assume that iron oxidation proceeds entirely heterogeneously, such that conventional approaches for determining ignition times based on gas phase species or temperature do not apply. For this reason, the present method - identifying ignition via the second derivative of the heat released during particle oxidation - is assumed to be a more appropriate choice. These ignition times are aligned with the qualitative observations described in Fig. 2. At τ_1 no significant temperature increase (red line) is observed, whereas at τ_2 there is widespread gas temperature rise. Thus, the first ignition stage can be attributed to the heating of nearby particles. Heat released by particle oxidation raises the local gas temperature T. This local temperature increase, particularly in regions with particle clustering (see Fig. 3), provides the heat required to heat-up nearby particles which can then ignite in the second stage. The second ignition stage then predominantly drives the subsequent rise in gas temperature. In the following sections, various parameters (see Table 1) are modified and the corresponding results are compared to the reference case in the same format as in Fig. 5.

4.2. Impact of gas temperature

Changing the initial gas temperature of the lower stream to a small value of $T_{LS} = 900$ K did not lead to ignition of the particle-laden mixing layer (not shown). Applying a slightly reduced value of $T_{LS} = 1200$ K, as shown in Fig. 6 - top, shifts the ignition times τ_1 and especially τ_2 to much later times, resulting in a delayed increase in T_{avg} and $\dot{Q}_t$. Notably, the trend of $d\dot{Q}_t$ shows two distinct local maxima with a stronger $\dot{Q}_t$ at τ_2. This phenomenon is attributed to the fact that the barely sufficient ignition energy at T_{LS} leads to the start of ignition of fewer particles (τ_1), whereas the heating of a large number of particles at τ_2 takes much more time, leading to a considerably delayed response, but eventually resulting in a stronger heat release rate. It is expected that for $900 < T_{LS} < 1200$ K, the second ignition time is shifted further towards later times until no oxidation can occur, as was found for the limiting case with $T_{LS} = 900$ K. The opposite effect is observed for $T_{LS} = 2000$ K in Fig. 6 - bottom, where the temperature is higher compared to the reference case. Both ignition times are slightly shifted to earlier times. Interestingly, the local maximum at τ_2 is nearly non-existent, showing that τ_1 and τ_2 are merging and leading to a steady rise in $\dot{Q}_t$.

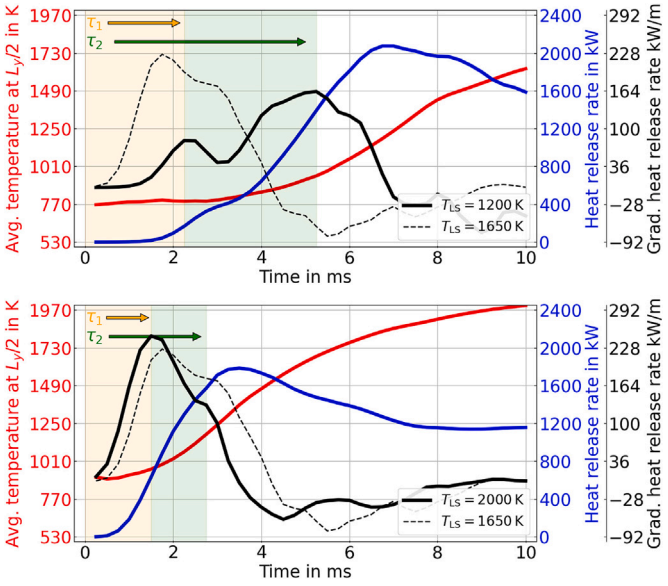

Fig. 6. Top: $T_{LS} = 1200$ K and bottom: $T_{LS} = 2000$ K. For all other plot labels see Fig. 5. (For interpretation of the references to colour in this figure legend, the reader is referred to the web version of this article.)

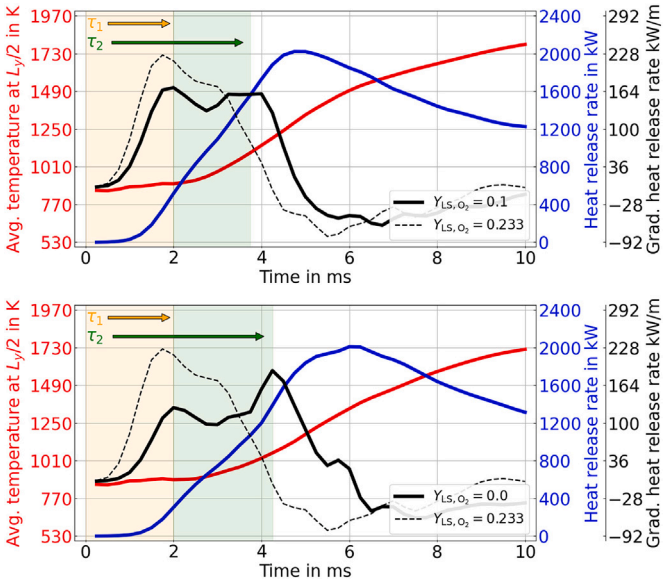

Fig. 7. Top: $Y_{LS,O_2} = 0.1$ and bottom: $Y_{LS,O_2} = 0.0$. For all other plot labels see Fig. 5. (For interpretation of the references to colour in this figure legend, the reader is referred to the web version of this article.)

4.3. Impact of oxygen mass fraction

A variation of the initial oxygen mass fraction in the lower stream is shown in Fig. 7, where the oxygen is gradually reduced from $Y_{LS,O_2} = 0.233$ to 0.1 (top) and 0.0 (bottom). In both cases with reduced oxygen,

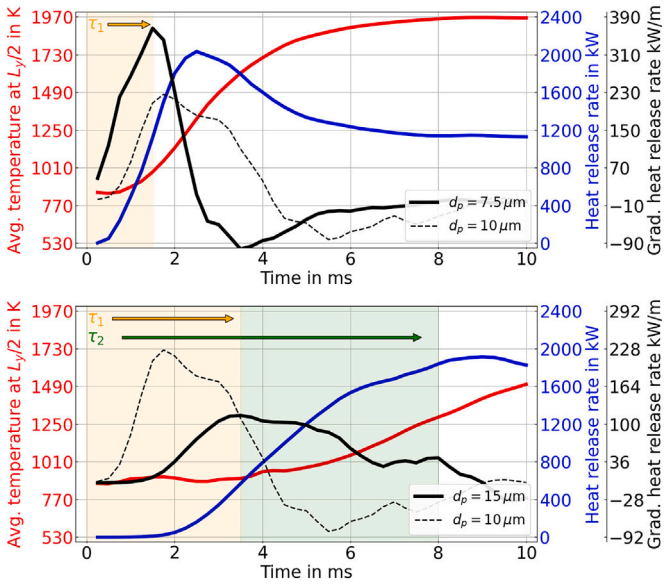

Fig. 8. Top: $d_p = 7.5\,\mu m$ and bottom: $d_p = 15\,\mu m$. For all other plot labels see Fig. 5 (Note that the y-axis for $d\dot{Q}_t$ has been extended compared to other plots.). (For interpretation of the references to colour in this figure legend, the reader is referred to the web version of this article.)

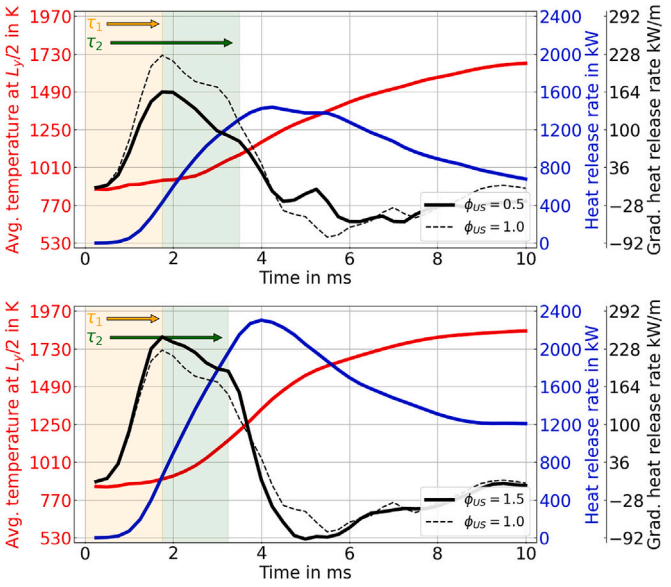

Fig. 9. Top: $\phi_{US} = 0.5$ and bottom: $\phi_{US} = 1.5$. For all other plot labels see Fig. 5. (For interpretation of the references to colour in this figure legend, the reader is referred to the web version of this article.)

the effect of two distinct ignition times is observed because of the limited availability of oxygen which slows down particle oxidation. However, the ignition events are only marginally shifted to later times. Both plots show that, contrary to initial expectations, particle oxidation in the mixing layer setup is mostly independent of the LS oxygen concentration, while the amount of oxygen in the US is likely more crucial. This indicates that the mixing process carries particles and oxygen together from the US to the LS, where they absorb the higher energy from the LS to initiate the oxidation process, while the added oxygen of the LS is less relevant. This will likely only change in extremely dense iron particle clouds or in combustor regions where fresh iron particles have entered a low-oxygen region.

4.4. Impact of the particle diameter

In Fig. 8 the particle diameter is varied while holding $\phi_{US} = \text{const.} = 1.0$ which induces an increased number of initial particles for $d_p < d_{p,\text{ref.}}$ and vice versa. In the case with a smaller $d_p = 7.5\,\mu m$ (Fig. 8 - top), only a single ignition time is observed, characterised by a strong and steady increase in the heat release rate that directly affects the gas temperature. Similar to the observation for the case with $T_{LS} = 2000\,K$, the two ignition times are now completely merged. The disappearance of the second ignition time can be attributed to the presence of more particles and the faster heating to the critical particle ignition temperature due to the smaller diameter, resulting in a faster heat release. In addition, turbulent clustering effects are stronger for particles with St $\rightarrow$ 1, further promoting rapid ignition. Consequently, the heat generated during the first stage increases so quickly that the second stage follows immediately, causing both stages to merge into a single event.

Increasing the particle diameter leads to the opposite effect due to the higher thermal inertia and fewer particles, as illustrated in Fig. 8 - bottom. The ignition times τ_1 and τ_2 are significantly delayed. The first ignition stage stretches over a much longer period of $1.5 < t < 6.75\,ms$, compared to the previously investigated cases. The reason for this behaviour is that larger particles ignite and release heat sequentially rather than simultaneously, a consequence also caused by the weaker influence of turbulent clustering. As a result of this process, the second ignition time is not initiated until $\tau_2 = 8\,ms$ with minimal impact.

4.5. Impact of the equivalence ratio

The results of varying the equivalence ratio ϕ_{US} based on the US are presented in Fig. 9. Decreasing the equivalence ratio from stoichiometric results in a reduced global fuel mass and therefore moderate heat release with a slower increase in the gas temperature, as shown in Fig. 9 - top. Conversely, an increase in ϕ would cause the opposite effect, up to the point where too much fuel mass is present ($\phi \gg 1$). However, observing the results in Fig. 9 - bottom, shows that a sufficient amount of oxygen is present which does not hinder the oxidation process at $\phi_{US} = 1.5$. This (non-)effect occurs because ϕ_{US} is based on the US only and does not account for the additional oxygen in the LS. Considering the previous findings from Section 4.3, we expect that reducing the availability of oxygen in the LS and simultaneously increasing ϕ_{US} would result in more pronounced effects.

4.6. Impact of fully-oxidised particles in the LS

In the context of iron particle oxidation and different from conventional hydrocarbon solid fuels (e.g. coal and biomass), fully-oxidised iron particles do not disappear but remain in the system as FeO. To explore this effect, two cases are investigated in which 25% and 50% of the initially present particles in the US are randomly added with $Y_{p,\text{FeO}} = 1.0$ and $T_{p,\text{FeO}} = T_{LS}$ to the LS indicated as $n_{p,\text{FeO}} = 25$ and $n_{p,\text{FeO}} = 50$ in Table 1. The results show (omitted for brevity) that the effect is minimal, with the profiles of T_{avg}, $\dot{Q}_t$ and $d\dot{Q}_t$ remaining very similar compared to the ref. case in Fig. 5. This is because the most prominent parameters affecting particle cloud ignition are T_{LS} (Section 4.2) and d_p (Section 4.4), which are not affected by the additional burnt-out particles. Since the latter do not react, they do not affect T_{LS} much, such that Fe particles entrained from the upper to the lower stream have a similar time evolution as the reference case.

4.7. Impact of radiation

Another parameter with uncertain impact is radiation. The results in Fig. 10 compare two cases with and without considering radiation. These results show that T_{avg} can be decreased by up to 10% while $\dot{Q}_t$ and $d\dot{Q}_t$ can increase by up to 10% for high temperatures ($> 1500\,K$). The somewhat higher values of $\dot{Q}_t$ and $d\dot{Q}_t$ may be explained by the

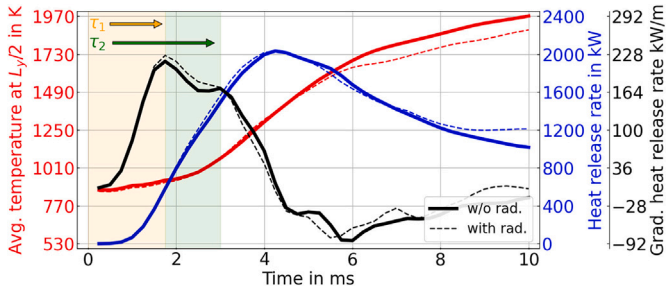

Fig. 10. Radiative comparison - for all other plot labels see Fig. 5. (For interpretation of the references to colour in this figure legend, the reader is referred to the web version of this article.)

Table 2
Results of our sensitivity analysis with increasing or decreasing ignition times (τ_1, τ_2), maximum relative deviation in percent ($\Delta^{\%}_{\max}$), and no (○), minor (●) and major (●) effects on particle self-ignition.

Parameter	Variation	τ_1	τ_2	$\Delta^{\%}_{\max}$	Effect
T_{LS}	↑ | ↓	↓ | ↑	↓ | ↑	75	●
$Y_{\mathrm{LS,O_2}}$	↓ | ↓↓	↑ | ↑	↑ | ↑	42	●
d_p	↑ | ↓	↑ | ↓	↑ | −	167	●
ϕ_{US}	↑ | ↓	= | ↑	= | ↑	17	●
$n_{p,\mathrm{FeO}}$	↓ | ↓↓	= | =	= | =	0	○
Rad.	off	=	=	0	○

↑: Increase, ↓: Decrease, ↓↓: Strong decrease, =: Unchanged, −: Absent
No ($\Delta^{\%}_{\max} = 0\%$), Minor ($0 < \Delta^{\%}_{\max} \leq 50\%$), Major ($\Delta^{\%}_{\max} > 50\%$).

fact that the heat released from individual particles is no longer concentrated locally, but is instead distributed more uniformly throughout the computational domain and heats up the surrounding particles. Despite this finding, it is important to note that the mixing layer in this study represents a canonical configuration without walls. Therefore, the radiation effects observed in this work cannot be directly transferred to real iron particle combustors, where far-away walls affect the intensities of incoming and outgoing radiation. In industrial combustors, where wall effects and different optical thicknesses are present, the impact of radiation on self-ignition may be more significant.

4.8. Summary of the results

To summarise our findings, an overview of the investigated cases and their major results is given in Table 2, with increasing or decreasing ignition times, maximum relative deviation and grey-scaled markers representing the effect of each parameter.

5. Conclusion

This study investigates the ignition behaviour of reacting iron particle clouds in sheared turbulence using CP-DNS. Starting with a reference case, various key quantities (T_{LS}, $Y_{\mathrm{LS,O_2}}$, d_p, ϕ_{US}, $n_{p,\mathrm{FeO}}$, radiation) have been varied to mimic different conditions that can occur in real iron combustors. The results revealed two distinct ignition stages with shifted times during iron combustion, where only the second stage affects the gas phase globally. These two stages could be identified for most conditions, but were absent in others. Under certain conditions, the first and second stages merge, leading to global cloud ignition at a single time. The parameters T_{LS} and d_p have a major impact on ignition, $Y_{\mathrm{LS,O_2}}$, and ϕ_{US} have a minor influence, while $n_{p,\mathrm{FeO}}$ and radiation show no considerable effect. The fundamental trends reported in this work may be used as a first indicator to control iron particle cloud combustion and to select optimised operating conditions for stable self-ignition in future iron particle combustors. Future work should also consider more detailed iron conversion sub-models to validate the findings from the present study.

CRediT authorship contribution statement

Tien Duc Luu: Writing – original draft, Visualization, Validation, Software, Methodology, Investigation, Formal analysis, Data curation, Conceptualization. **Marlon Göhringer:** Writing – review & editing, Visualization, Software, Methodology, Investigation, Formal analysis, Data curation. **David Märker:** Writing – review & editing, Software, Methodology. **Oliver T. Stein:** Writing – review & editing, Supervision, Resources, Project administration, Funding acquisition, Conceptualization.

Declaration of competing interest

The authors declare that they have no known competing financial interests or personal relationships that could have appeared to influence the work reported in this paper.

Acknowledgements

This work is conducted within the *Clean Circles* research initiative. O.T. Stein gratefully acknowledges support by the Helmholtz Association of German Research Centres (HGF), within the research field *Energy*, program *Materials and Technologies for the Energy Transition (MTET)*. The authors acknowledge support by the state of Baden-Württemberg for HPC time through bwHPC.

Data availability

Data will be made available on request.

References

[1] Bergthorson JM. Recyclable metal fuels for clean and compact zero-carbon power. Prog Energy Combust Sci 2018;68:169–96.
[2] Debiagi P, Rocha RC, Scholtissek A, Janicka J, Hasse C. Iron as a sustainable chemical carrier of renewable energy: analysis of opportunities and challenges for retrofitting coal-fired power plants. Renew Sustain Energy Rev 2022;165:112579.
[3] Goroshin S, Bidabadi M, Lee JHS. Quenching distance of laminar flame in aluminum dust clouds. Combust Flame 1996;105:147–60.
[4] Soo M, Goroshin S, Bergthorson JM, Frost DL. Reaction of a particle suspension in a rapidly-heated oxidizing gas. Prop Expl Pyrotechn 2015;40:604–12.
[5] Hazenberg T, van Oijen JA. Structures and burning velocities of flames in iron aerosols. Proc Combust Inst 2021;38:4383–90.
[6] Thijs LC, van Gool CEAG, Ramaekers WJS, Kuerten JGM, van Oijen JA, de Goey LPH. Improvement of heat- and mass transfer modeling for single iron particles combustion using resolved simulations. Combust Sci Technol 2022;1:1–17.
[7] Mich J, Braig D, Gustmann T, Hasse C, Scholtissek A. A comparison of mechanistic models for the combustion of iron microparticles and their application to polydisperse iron-air suspensions. Combust Flame 2023;256:112949.
[8] Tang F-D, Higgins AJ, Goroshin S. Propagation limits and velocity of reaction-diffusion fronts in a system of discrete random sources. Phys Rev E 2012;85:036311.
[9] Lam F, Mi X, Higgins AJ. Front roughening of flames in discrete media. Phys Rev E 2017;96:013107.
[10] Vance FH, Scholtissek A, Nicolai H, Hasse C. Flame propagation modes for iron particle clusters in air, part II: transition from continuous to discrete propagation mode under strong convection effects. Combust Flame 2024:113199.
[11] Ravi A, de Goey P, van Oijen J. Flame structure and burning velocity of flames propagating in binary iron aerosols. Proc Combust Inst 2023;39:3573–81.
[12] Wen X, Scholtissek A, van Oijen J, Bergthorson J, Hasse C. Numerical modeling of pulverized iron flames in a multidimensional hot counterflow burner. Combust Flame 2023;248:112572.
[13] Luu TD, Shamooni A, Kronenburg A, Braig D, Mich J, Nguyen B-D, Scholtissek A, Hasse C, Thäter G, Carbone M, Frohnapfel B, Stein OT. Carrier-phase DNS study of particle size distribution effects on iron particle ignition in a turbulent mixing layer. Proc Combust Inst 2024;40:105297.
[14] Thäter G, Carbone M, Luu TD, Stein OT, Frohnapfel B. The influence of clustering in homogeneous isotropic turbulence on the ignition behavior of iron particles. Proc Combust Inst 2024;40:105348.
[15] Hemamalini S, Cuenot B, van Oijen J, Mi XC. Numerical study probing the effects of preferential concentration on the combustion of iron particles in a mixing layer. Proc Combust Inst 2024;40:105617.
[16] Nguyen BD, Scholtissek A, Li T, Ning D, Stein OT, Dreizler A, Hasse C. Nanoparticle formation in the boundary layer of burning iron microparticles: modeling and simulation. Chem Eng J 2025;507:160039.
[17] Ning D, Shoshin Y, van Oijen JA, Finotello G, de Goey LPH. Burn time and combustion regime of laser-ignited single iron particle. Combust Flame 2021;230:111424.

[18] Panahi A, Chang D, Schiemann M, Fujinawa A, Mi X, Bergthorson JM, Levendis YA. Combustion behavior of single iron particles-Part I: an experimental study in a drop-tube furnace under high heating rates and high temperatures. Appl Energy Combust Sci 2023;13:100097.
[19] Fedoryk M, Stelzner B, Harth S, Trimis D. Experimental investigation of the laminar burning velocity of iron-air flames in a tube burner. Appl Energy Combust Sci 2023;13:100111.
[20] Hulsbos MR, Hermanns RTE, Bastiaans RJM, de Goey L. The heat flux method for hybrid iron–methane–air flames. Combust Flame 2024;266:113531.
[21] Hameete J, Boone LJ, Homan TAM, Shoshyn Y, Dam NJ, de Goey LPH. Aerosol ignition in iron powder flames stabilized on a new type of jet-in-hot-coflow burner. Appl Energy Combust Sci 2024;20:100301.
[22] Luu TD, Shamooni A, Kronenburg A, Braig D, Mich J, Nguyen B-D, Scholtissek A, Hasse C, Thäter G, Carbone M, Frohnapfel B, Stein OT. Carrier-Phase DNS of ignition and combustion of iron particles in a turbulent mixing layer. Flow Turb Combust 2024;112:1083–103.
[23] Chase MW. NIST-JANAF thermochemical tables. 4th ed. vol. 9. Gaithersburg: Am. Inst. Phys.; 1998.
[24] Thijs LC, van Gool CEAG, Ramaekers WJS, van Oijen JA, de Goey LPH. Resolved simulations of single iron particle combustion and the release of nano-particles. Proc Combust Inst 2023;39:3551–9.
[25] Sirignano WA. Fluid dynamics and transport of droplets and sprays. 2nd ed. Cambridge University Press; 2010.
[26] Zhifu Z, Guoxiang W, Bin C, Liejin G, Yueshe W. Evaluation of evaporation models for single moving droplet with a high evaporation rate. Powder Technol 2013;240:95–102.
[27] Sontheimer M, Kronenburg A, Stein OT. Two-phase coupling for MMC-LES of spray combustion. Proc Combust Inst 2021;38:3361–9.
[28] Rieth M, Kempf AM, Kronenburg A, Stein OT. Carrier-phase DNS of pulverized coal particle ignition and volatile burning in a turbulent mixing layer. Fuel 2018;212:364–74.
[29] Shamooni A, Debiagi P, Wang B, Luu TD, Stein OT, Kronenburg A, Bagheri G, Stagni A, Frassoldati A, Faravelli T, Kempf AM, Wen X, Hasse C. Carrier-phase DNS of detailed NO_x formation in early-stage pulverized coal combustion with fuel-bound nitrogen. Fuel 2021;291:119998.
[30] Wang B, Shamooni A, Stein OT, Kronenburg A, Kempf AM, Debiagi P, Hasse C. Investigation of turbulent pulverized solid fuel combustion with detailed homogeneous and heterogeneous kinetics. Energy Fuels 2021;35:7077–91.
[31] Mi X, Fujinawa A, Bergthorson JM. A quantitative analysis of the ignition characteristics of fine iron particles. Combust Flame 2022;240:112011.
[32] van Gool CEAG, Thijs LC, Ramaekers WJS, van Oijen JA, de Goey LPH. Particle equilibrium composition model for iron dust combustion. Appl Energy Combust Sci 2023;13:100115.
[33] Mich J, da Silva AK, Ning D, Li T, Raabe D, Böhm B, Dreizler A, Hasse C, Scholtissek A. Modeling the oxidation of iron microparticles during the reactive cooling phase. Proc Combust Inst 2024;40:105538.
[34] O'Brien J, Urzay J, Ihme M, Moin P, Saghafian A. Subgrid-scale backscatter in reacting and inert supersonic hydrogen-air turbulent mixing layers. J Fluid Mech 2014;743:554–84.
[35] Hilbert R, Thévenin D. Autoignition of turbulent non-premixed flames investigated using direct numerical simulations. Combust Flame 2002;128:22–37.